Structure and principles of self-assembly of giant "sea urchin" type sulfonatophenyl porphine aggregates

Marijus Pleckaitis[1,2], Fayez Habach[3], Lukas Kontenis[1,4], Gábor Steinbach[5,6,7], Greta Jarockyte[1,2], Agne Kalnaityte[1], Ildikó Domonkos[8], Parveen Akhtar[8], Mehdi Alizadeh[1], Saulius Bagdonas[1], Vitalijus Karabanovas[1,2,9], Győző Garab[7,8,10], Ricardas Rotomskis[1,2], and Virginijus Barzda[1,3,11] (✉)

[1] Laser Research Center, Faculty of Physics, Vilnius University, Sauletekio av. 10, Vilnius LT-10223, Lithuania
[2] Biomedical Physics Laboratory, National Cancer Institute, P. Baublio str. 3b, Vilnius LT-08406, Lithuania
[3] Department of Chemical and Physical Sciences, University of Toronto Mississauga, 3359 Mississauga Rd, Mississauga L5L 1C6, Canada
[4] Light Conversion, Keramiku str. 2B, Vilnius LT-10233, Lithuania
[5] Cellular Imaging Laboratory, Biological Research Centre, Eötvös Loránd Research Network, Temesvári körút 62, Szeged 6726, Hungary
[6] Institute of Biophysics, Biological Research Centre, Eötvös Loránd Research Network, Temesvári körút 62, Szeged 6726, Hungary
[7] Biofotonika Research and Development Ltd., Dózsa u. 7, Szeged 6720, Hungary
[8] Institute of Plant Biology, Biological Research Centre, Eötvös Loránd Research Network, Temesvári körút 62, Szeged 6726, Hungary
[9] Department of Chemistry and Bioengineering, Vilnius Gediminas Technical University, Sauletekio av. 11, Vilnius LT-10223, Lithuania
[10] Department of Physics, Faculty of Science, University of Ostrava, Chittussiho 10, Ostrava CZ-710 00, Czech Republic
[11] Department of Physics, University of Toronto, 60 St. George St. Toronto, Toronto M5S 1A7, Canada

ABSTRACT

Principles of molecular self-assembly into giant hierarchical structures of hundreds of micrometers in size are studied in aggregates of meso-tetra(4-sulfonatophenyl)porphine (TPPS$_4$). The aggregates form a central tubular core, which is covered with radially protruding filamentous non-branching aggregates. The filaments cluster and orient at varying angles from the core surface and some filaments form bundles. Due to shape resemblance, the structures are termed giant sea urchin (GSU) aggregates. Spectrally resolved fluorescence microscopy reveals J- and H-bands of TPPS$_4$ aggregates in both the central core and the filaments. The fluorescence of the core is quenched while filaments exhibit strong fluorescence. Upon drying, the filament fluorescence gets quenched while the core is less affected, showing stronger relative fluorescence. Fluorescence-detected linear dichroism (FDLD) microscopy reveals that absorption dipoles corresponding to J-bands are oriented along the filament axis. The comparison of FDLD with scanning electron microscopy (SEM) reveals the structure of central core comprised of multilayer ribbons, which wind around the core axis forming a tube. Polarimetric second-harmonic generation (SHG) and third-harmonic generation microscopy exhibits strong signal from the filaments with nonlinear dipoles oriented close to the filament axis, while central core displays very low SHG due to close to centrosymmetric organization. Large chiral nonlinear susceptibility points to helical arrangement of the filaments. The investigation shows that TPPS$_4$ molecules form distinct aggregate types, including chiral nanotubes and nanogranular aggregates that associate into the hierarchical GSU structure, prototypical to complex biological structures. The chiral TPPS$_4$ aggregates can serve as harmonophores for nonlinear microscopy.

KEYWORDS

meso-tetra(4-sulfonatophenyl)porphine (TPPS$_4$) aggregates, self-assembly, nanostructures, harmonophores, polarimetric second harmonic generation microscopy, third harmonic generation microscopy

1   Introduction

Molecular self-assembly is a spontaneous process that governs the formation of ordered aggregates. It plays a key role in abiogenesis, a natural process by which life arose from simple organic compounds [1]. In particular, meso-tetra(4-sulfonatophenyl) porphine (TPPS$_4$) has been widely studied due to its ability to form noncovalently bound supramolecular structures [2, 3]. The best known structures are highly ordered cylindrical/helical J-aggregates of TPPS$_4$ molecules [4, 5]. In addition, flat or flocculated structures of the aggregates can be formed [6]. Self-assembly of TPPS$_4$ molecules strongly depends on the composition of the solution and various external factors. Physical forces in the solution, such as vortex stirring or spinning, can induce chiral assembly of TPPS$_4$ aggregates [7]. The structure of aggregates strongly depends on the functional groups of porphyrin molecules as well as on the inserted metal ions [8, 9]. The chiral assembly of TPPS$_4$ aggregates can be controlled by the addition of chiral templates such as DNA [10, 11], amino acids [12, 13], polypeptides [14, 15], gelators [16], or other organic templates [17, 18]. Numerous applications have been developed for TPPS$_4$ and other porphyrin aggregates including humidity

biosensors [19], artificial light energy harvesting and transfer systems [20, 21], and photodynamic therapy agents [22, 23]. While most studies are conducted on homogeneous aggregates of hundreds of nanometers in size, differently ordered aggregates can further interact and assemble into complex hierarchical structures characteristic of living organisms [6, 24–29]. The self-organization of TPPS$_4$ molecules into higher complexity hierarchical microstructures is not well understood and is the focus of this study.

In this paper, we investigate giant self-assembled TPPS$_4$ aggregates in aqueous acidic solution. The aggregates are hundreds of micrometers to several millimeters in size and possess structures resembling the shape of sea urchins, and therefore, named giant sea urchin (GSU) aggregates. A suite of various microscopy techniques is applied for investigation of GSU TPPS$_4$ aggregates. A spectrally resolved confocal fluorescence microscopy can probe aggregate organization by selectively exciting J-band with the 488 nm light, or using 405 and 420 nm to excite predominantly ionic form and H-band, respectively. The fluorescence spectra of TPPS$_4$ aggregates depend on the aggregate ultrastructure, and environmental conditions, e.g., hydration [30] and ionic strength [31]. TPPS$_4$ aggregates embedded in micelles have a distinct fluorescence peak at 714 nm assigned to J-aggregates, and peaks at 670 and 720 nm assigned to H-aggregates [3]. Spectrally-resolved fluorescence imaging allows to discriminate the differently arranged parts of GSU structures.

The fluorescence lifetime imaging microscopy (FLIM) is a powerful tool to investigate quenching and energy transfer in the aggregates [32–34], and it can discern different organization and heterogeneity [35] of the aggregates. Short fluorescence lifetimes, around 1 ns, are observed in the needle-like TPPS$_4$ aggregates protruding from the core-shell polyelectrolyte structure at pH 3 [27]. The filaments of GSU TPPS$_4$ aggregates studied in this work resemble the above-mentioned needle-like structures.

The ultrastructural arrangement of TPPS$_4$ molecules in the aggregates can be probed with polarization-resolved microscopy in either linear or nonlinear optical regime. In the linear regime, we used fluorescence-detected linear dichroism (FDLD) microscopy that measures normalized difference of fluorescence intensity excited with linearly polarized light at two perpendicular orientations [36–38]. FDLD microscopy has been applied to map the spatial orientation of absorption dipoles, which revealed highly anisotropic and homogeneously aligned porphyrin aggregates in artificial chlorosomes, resembling light harvesting antenna of green photosynthetic bacteria [21].

Nonlinear optical properties and the ultrastructure of GSU aggregates are further explored using polarimetric second- and third-harmonic generation (SHG, THG) microscopy [39]. The reduced SHG polarimetry with linear polarization-in polarization-out (PIPO) method is employed to determine the ultrastructure of aggregates, in terms of achiral and chiral nonlinear susceptibility tensor components ratios, as well as in-image-plane and out-of-plane cylindrical axis orientation and filament polarity within voxels of the image [40, 41]. The PIPO SHG measurements also provide with the degree of linear polarization that characterizes disorder in the samples [42].

This study shows that TPPS$_4$ molecules can form several structural types of aggregates in the same solution that interact with each other and assemble into hierarchical assemblies resembling sea urchins. The principles governing hierarchical self-assembly in TPPS$_4$ aggregates may have played a role at the early stages of abiogenesis. Similar principles of the hierarchical aggregate formation can be used to design structures for light harvesting in artificial photosynthesis [21], sensing [43], molecular plasmonics [44], and molecular electronics [45]. The aggregates can be employed as harmonophores for nonlinear microscopy [46, 47].

2 Experimental

2.1 Materials

TPPS$_4$ was purchased from Sigma Aldrich (St. Louis, Missouri, USA) and used without further purification. For sample immobilization, the GSU TPPS$_4$ aggregates were trapped in a polyacrylamide gel [48]. Acrylamide, 98+%, N,N'-Methylenebisacrylamide, 97%, Ammonium peroxydisulfate, APS, 98.0% min, and N,N,N',N'-Tetramethylethylenediamine (TEMED), 99%, were all purchased from Thermo Fisher Scientific (Waltham, Massachusetts, USA).

2.2 Sample preparation

A 10^{-3} M stock solution of TPPS$_4$ was prepared by dissolving porphyrin powder in distilled water. The macroscopic supramolecular structures self-assembled in the solution prepared by diluting the stock to 2×10^{-5} M with 0.1 M aqueous HCl solution, i.e., 1 mL of the stock solution was added into 49 mL of 0.1 M aqueous HCl solution and mixed randomly. The solutions of 50 mL in volumes were aged in tightly closed glass containers in the dark at room temperature for more than a year. For microscopy imaging, the "wet" GSU supramolecular TPPS$_4$ aggregates were mounted in the original aggregation medium, or mixed with a polyacrylamide gel components and gelled on a microscope glass slide after covering with a cover slip. The gel was made from 5% acrylamide: bis-acrylamide (30:1), polymerized with 0.5% ammonium persulfate, and 0.5% TEMED [48]. The "dry" GSU samples were prepared by air-drying the aqueous aggregates deposited with the aggregation medium onto a cover slip.

2.3 Brightfield and spectral confocal fluorescence microscopy

Brightfield and differential interference contrast (DIC) microscopy was used to visualize morphological characteristics of the TPPS$_4$ aggregates. Images were recorded either with 20×/NA 0.5 or 40×/NA 0.95 objectives (Plan Fluor, Nikon, Japan) by using a CCD camera (Nikon DS-Fi2). Samples of GSU aggregates were analyzed with a confocal laser scanning microscope (Nikon Eclipse TE2000-S, C1 plus, Nikon, Japan) equipped with a fiber coupled spectrometer (QE65000 Ocean Optics, Inc., UK). The transmittance and confocal fluorescence imaging was carried out using a 404 nm diode laser or a 488 nm beam from an argon ion laser. Fluorescence emission was detected using a 688/134 nm band-pass filter (Semrock Inc., USA). The image acquisition was controlled by the Nikon EZ-C1 software. The images were further processed using EZ-C1 v3.91 (Nikon, Japan) and ImageJ v1.53a software (NIH, USA) [49].

2.4 Fluorescence lifetime imaging microscopy

Fluorescence lifetime images were acquired using a Lifetime and Fluorescence Correlation Spectroscopy Upgrade (hardware) for Nikon C1si (PicoQuant GmbH, Berlin, Germany) confocal microscopes. Excitation was provided by a Fianium WhiteLase Micro supercontinuum laser (NKT Photonics, Birkerød, Denmark) with a pulse repetition rate of 30 MHz. Spectral ranges were selected from the supercontinuum using 420/10 and 490/10 nm band-pass filters (Thorlabs Inc., Newton, New Jersey, USA) for specific excitation of TPPS$_4$ H- and J-aggregates, respectively. The fluorescence photons were detected after a 620 nm longpass filter (Thorlabs Inc.) using a single-photon-counting avalanche photodiode (SPAD) (Micro Photon Devices, Bolzano, Italy) and counted by a time-correlated single-photon

counter PicoHarp 300 (PicoQuant GmbH). Each lifetime image was obtained by collecting on average 500 counts/pixel, and the image size was fixed at 512 pixel × 512 pixel. FLIM images were constructed using SymPhoTime 64 software (PicoQuant GmbH), in which amplitude weighted average fluorescence lifetime of TPPS$_4$ aggregates was determined at every pixel. Distributions of fluorescence lifetimes were plotted using SymPhoTime 64 v.2.4.4874 software (PicoQuant GmbH).

2.5 Fluorescence-detected linear dichroism microscopy

The fluorescence-detected linear dichroism imaging was done using a DP-RCM [50]. The Re-scan Confocal Microscope [51] (RCM, Confocal.nl, Netherlands) was attached to a Nikon Inverted Eclipse Ti fluorescence microscope (Nikon Instruments Inc., Japan). The excitation laser (Cobolt 30 mW 488 nm diode laser, 0488–06–03–0030–200, Cobolt AG, Sweden) light was modulated by a liquid crystal (LC) retarder (LCC1115-A, Thorlabs, Germany) in order to generate vertically- and horizontally-polarized light for subsequent images. A 40×/NA 0.60 air objective was used. Fluorescence was selected by a quad-band dichroic and emission filters (ZT405/488/561/640rpc and ZET405/488/561/640m, respectively; Chroma Technology Corp., USA). The images were collected by a sCMOS camera (Andor Zyla 4.2 PLUS, Oxford Instruments, UK) using NIS-Elements BR software (version: 4.60.00, Nikon Instruments Inc., Japan) and post processed by custom routine written in Matlab [50].

2.6 Scanning electron microscopy

A drop of sample was air dried on a 5 mm × 5 mm glass cover slip, mounted on a scanning electron microscopy stub and covered with 5 nm gold by a Quorum Q150T ES sputter and then observed in a JEOL JSM-7100F/LV scanning electron microscope (JEOL Ltd., Japan). Specimens were imaged by detecting secondary electrons at 3 kV accelerating voltage.

2.7 Atomic force microscopy

The Innova® Atomic Force Microscope (AFM) (Bruker Corporation, Billerica, Massachusetts, USA) with SPMLab software version 7.11 was used to image the dry GSU aggregates. The GSU aggregates were placed on a glass substrate, air dried, and used for fluorescence microscopy as well as AFM imaging. Samples were scanned in the tapping mode with a point probe silicon tip of < 15 nm radius (model: TESPA) (Bruker Corporation), and oscillation frequency of 230–410 kHz was applied. Topographic images of 5 μm × 5 μm were acquired at a scan rate of 2 Hz, containing 512 pixel × 512 pixel.

2.8 Multimodal second- and third-harmonic generation microscopy

Second and third harmonic-generation images were acquired using a home-built laser-scanning microscope coupled to a solid-state femtosecond oscillator (Light Conversion FLINT, Light Conversion, Vilnius, Lithuania), emitting sub-100 fs pulses at 76 MHz with a central wavelength of 1,030 nm. The excitation beam at the entrance of the excitation objective (Nikon CFI Plan Apo Lambda 20×/NA 0.75) was linearly polarized at 45° with respect to the horizontal image axis. The harmonic signal was collected using a plano-convex singlet lens with an effective NA of 0.5. SHG and THG signals were separated by a dichroic mirror (DMLP505R, Thorlabs) and filtered using combination of FBH520/40 and FGB39 and FGUV11 (all from Thorlabs) filters, respectively, before reaching the photon-counting PMT detectors (Hamamatsu H10682–210). The sample was translated axially in *Z* direction using a DC-servo stage (ASI LS-50). Laser scanning,

sample stepping in axial direction and data acquisition was performed in LabView (National Instruments Corporation, Austin, Texas, USA). Images with a field size of 780 μm were scanned at 1 μm pixel resolution at 20 μs dwell time, the Z stack frames were recorded at 5 μm step over a range of 210 μm. Data analysis and 3D rendering was carried out using Python and Fiji [52].

2.9 Polarimetric second-harmonic generation microscopy

The polarimetric second harmonic generation (P-SHG) microscope was used with linear PIPO configuration [53]. Excitation was provided by a home-made oscillator based on an Yb-ion-doped potassium gadolinium tungstate (Yb:KGW) crystal. The laser provided ~ 430 fs pulses at 1,028 nm peak wavelength and 14.3 MHz pulse repetition rate [54]. The laser was coupled to a home-built laser scanning microscope, which contains a polarization state generator (PSG) for the incident laser beam and a polarization state analyzer (PSA) to measure the polarization state of the SHG signal detected in the forward direction (transmission configuration). The PSG contains a linear polarizer (Laser Components Inc.) and a half-wave plate (Comar Optics). The PSG is placed before the excitation objective (20×/NA 0.75 air objective (Carl Zeiss)). The PSA is placed after a custom 0.85 NA collection objective and contains a rotating linear polarizer. The SHG signal is filtered from the fundamental beam with a Schott BG 39 glass filter and a 510–520 nm band-pass interference filter (Edmund Optics) placed in front of a single-photon counting photomultiplier tube (Hamamatsu H7422P-40). To perform PIPO imaging, the PSG half-wave plate was rotated to nine different angles with equal increments from 0° to 180°, while the PSA was rotated to nine different evenly spaced angles from 0° to 180° for each PSG state. Regions of interest (ROI) of 110 μm × 110 μm were scanned with 2 μs dwell time, and 50 frames to 100 frames of 128 pixel × 128 pixel were summed to obtain an image for each polarization state configuration. The PIPO analysis was performed with custom software written in Matlab [50].

2.10 Modelling of TPPS$_4$ aggregates

Models were made with Avogadro v1.2.0: an open-source molecular builder and visualization tool [55].

3 Results

3.1 Laser scanning confocal and spectrally resolved fluorescence microscopy

Different shapes of TPPS$_4$ aggregates were investigated with confocal laser scanning microscopy (Fig. 1). Additionally, TPPS$_4$ aggregates were imaged using brightfield and DIC microscopy (Fig. S1 in the Electronic Supplementary Material (ESM)). Some of the TPPS$_4$ aggregates formed peculiar giant structures resembling sea urchins. The GSU structure reveals two distinct formations of the aggregates: (i) the central core with a diameter of 20 to 30 μm (for different GSU aggregates) and hundreds of micrometers long (Figs. 1(a)–1(d)); (ii) the filaments resembling hair or cilia that protrude from the central core surface with various tilt angles (see Figs. 1(a) and 1(c)). The same tilt is observed for large clusters or layers of the filaments that cross each other at different heights (Figs. 1(a) and 1(c)). Some filaments also bend and cluster along the central core surface (Fig. 1(a)). The filaments are non-branching, but some stick together forming bundles (Fig. 1(c)).

The transmission images of GSU aggregates show strong absorption at 404 nm in the central core and weaker absorption in the filaments (Figs. 1(a) and 1(c)), while the absorption is very
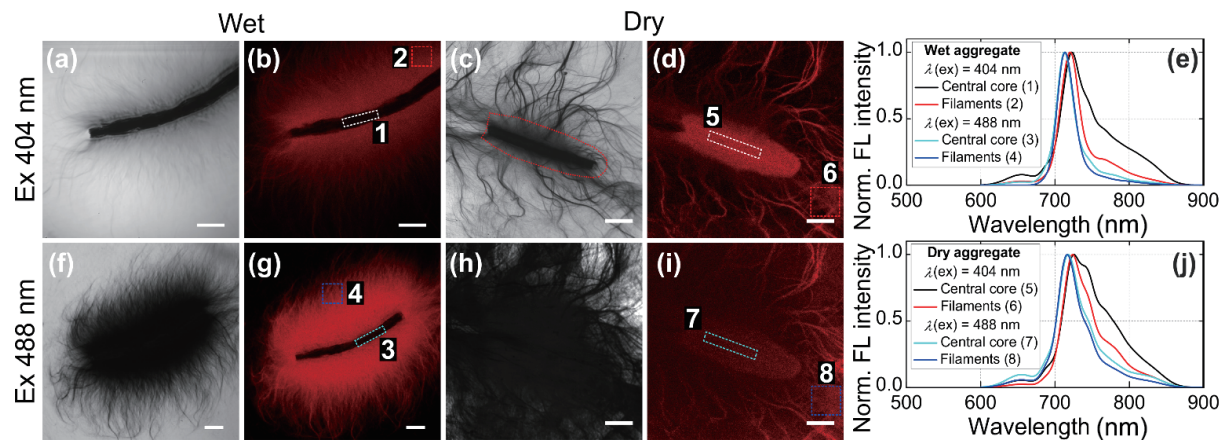
Figure 1 Spectrally-resolved confocal fluorescence microscopy of wet ((a), (b), (f), and (g)) and dry ((c), (d), (h), and (i)) GSU TPPS$_4$ aggregates. The transmission ((a), (c), (f), and (h)) and fluorescence ((b), (d), (g), and (i)) images obtained at 404 ((a)–(d)) and 488 nm ((f)–(i)) excitation. The normalized fluorescence spectra are shown for wet (e) and dry (j) aggregates obtained from numbered regions (core: 1, 3, 5, 7, filaments: 2, 4, 6, 8) in the images. The Gaussian decompositions of the spectra are presented in the Figs. S2–S9 in the ESM. Scale bars: 50 μm.

strong in filaments at 488 nm (Figs. 1(f) and 1(h)) and overshadows the core. The fluorescence images reveal the core structure in GSU aggregates (Figs. 1(g) and 1(i)). In wet aggregates, the core appears less fluorescent than the filaments (Figs. 1(b) and 1(g)).

In contrast, the dry GSU aggregates show distinct fluorescence of the core (Figs. 1(d) and 1(i)), which appears wider than in the transmission images (compared with Figs. 1(c) and 1(h)). The upper layer of the core and the surrounding layer of elevated filaments sloping down towards the substrate give the core wider appearance in the fluorescence images of dry aggregates (Figs. 1(d) and 1(i)).

Spectral data show the dependence of fluorescence bands on the excitation wavelengths. Under 404 nm excitation of the ionic form and the blue shifted H-band, the dominant fluorescence component peaks at 724 nm (Table 1). The red shifted fluorescing species (743 and 768 nm) also show substantial contribution with stronger signal from the central core, while fluorescence at 711 nm is relatively low. The direct excitation of J-band at 488 nm results in distinctly higher fluorescence at 711 nm, while the fluorescence peaking at 724 nm, as well as at 743 and 768 nm, remains relatively low. The observed changes in fluorescence spectra reveal that the GSU structure is heterogeneous and combines properties of both J- and H-aggregates.

The presence of all fluorescence components at different excitation wavelength indicates the connectivity between these different molecular arrangements.

When comparing spectra of wet and dry samples under the corresponding excitation conditions, the fluorescence typical for J-aggregates is more pronounced in the wet aggregates. In contrast, the fluorescence of H-aggregates and red-shifted species dominates in dry samples.

Comparison of the central core and the filaments reveals similar contributions from the spectral component patterns associated with J- and H-aggregates to the fluorescence spectra obtained under the same excitation and wet/dry conditions. The red shifted fluorescence at 743 and 768 nm is substantially present in the central core regardless of the excitation wavelength, while this fluorescence is almost absent in the wet filaments. In the dry samples, the red shifted fluorescence is particularly strong in the central core at 404 nm excitation. Therefore, red shifted 743 and 768 nm fluorescing species can be ascribed to the aggregate forms specific for the central core.

3.2 Time resolved fluorescence microscopy

Fluorescence lifetime imaging microscopy is performed on the wet and dry GSU aggregates using 420 and 490 nm excitation (Fig. 2). The FLIM images are shown in Figs. 2(a)–2(d), with average fluorescence lifetimes from 0.2 to 0.9 ns. The average lifetime distributions over the ROIs are given in Fig. 2(f). The fit parameters of 3-exponential fluorescence decays of ROIs (Fig. S10 in the ESM) for all aggregates are presented in Table S1 in the ESM.

Comparison between the four FLIM images and average lifetime distributions (Fig. 2) reveals the longest average lifetimes present in the wet aggregates at 420 nm excitation, where the lifetimes can be attributed predominantly to patterns of H-aggregates and red-shifted fluorescing species. Under direct

Table 1 Gaussian decomposition of fluorescence spectra for the wet and dry GSU aggregates

Sample, λ (ex)	ROI		A1[a] (691 nm)	A2[a] (711 nm)	A3[a] (724 nm)	A4[a] (743 nm)	A5[a] (768 nm)
Wet, 404 nm	1	C[b]	0.125	0.41	0.77	0.54	0.39
	2	F[b]	0.06	0.5	0.755	0.21	0.18
Wet, 488 nm	3	C[b]	0.12	0.865	0.33	0.17	0.085
	4	F[b]	0.05	0.83	0.38	0.10	0.055
Dry, 404 nm	5	C[b]	0.13	0.315	0.77	0.77	0.55
	6	F[b]	0.075	0.355	0.80	0.61	0.335
Dry, 488 nm	7	C[b]	0.18	0.68	0.64	0.45	0.23
	8	F[b]	0.15	0.73	0.59	0.40	0.17

[a] Amplitudes of Gaussian components of fluorescence spectra. Numbers in the brackets show the Gaussian component peak wavelength. The spectra are normalized to the most intense peak, and amplitudes represent the relative contributions of each fluorescing species. [b] The central core is abbreviated as C and the filaments as F.
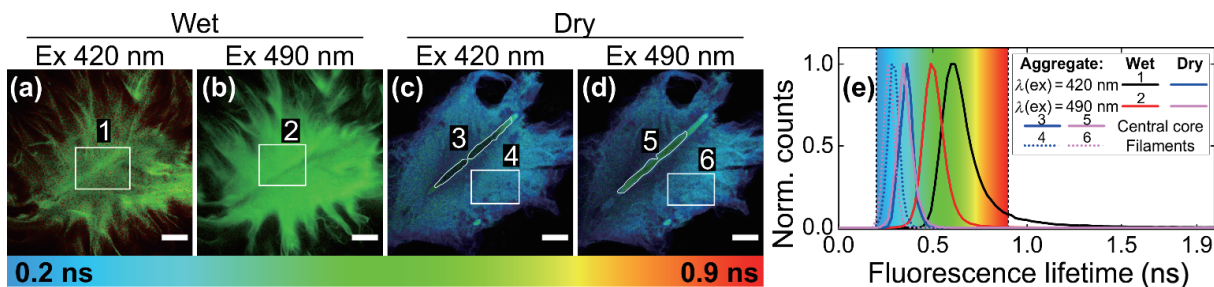
Figure 2 Fluorescence lifetime images of the wet and dry TPPS$_4$ aggregates under 420 nm ((a) and (c)) and 490 nm laser excitations ((b) and (d)). Images in panels (a)–(d) have a shared fluorescence lifetime colorbar. Distributions of the amplitude-weighted average fluorescence lifetimes (e), with figure legend showing the wet/dry conditions and excitation wavelength. The color background of the graph (e) has the corresponding range of the colors ((a)–(d)) representing fluorescence lifetimes 0.2–0.9 ns. Scale bars: 100 μm.

excitation of the spectral components of J-aggregates with 490 nm, the fluorescence decays become faster. This appears due to slightly shorter J-aggregate lifetimes [56] that determine the overall fluorescence decays of connected aggregates.

When the GSU aggregate is air dried and the filaments get packed on each other on a substrate, the core slightly flattens (see SEM images in Figs. 4(c) and 4(d), and AFM images in Fig. 5). Consequently, the average fluorescence lifetimes shorten significantly and all the three fluorescence decay components get affected (see Table S1 in the ESM), providing the evidence for fluorescence quenching. The spectral and time resolved fluorescence indicates that quenching most strongly affects spectral component pattern of J-aggregates upon drying.

The comparison of fluorescence lifetimes in the core and the filaments reveals that the shortest lifetimes are in the dry filaments. The quenching of the core is less pronounced upon drying compared to the filaments. Therefore, the core appears dark in the wet GSU aggregate fluorescence images (Figs. 1(b) and 1(g)), but emerges as a fluorescent structure in the dry aggregate (Figs. 1(d) and 1(i)). The FLIM microscopy exposes connectivity in TPPS$_4$ aggregates, which is an important property for applications of light harvesting in artificial photosynthesis. Studies on exciton-exciton annihilation may give further details on energy transfer domains in the GSU aggregates [57].

3.3 Fluorescence-detected polarization microscopy

The absorption dipole orientations of J-aggregates in the GSU structure were probed by FDLD imaging using 488 nm excitation [50]. The central core shows stripes with dipoles oriented parallel and perpendicular to the axis of the core (Fig. 3). Different dipole orientations reflect the heterogeneous organization of TPPS$_4$ core. Note that the absorption dipoles of the filaments attached to the core surface also contribute to the FDLD image.

The dipoles of J-bands in the filaments are organized along the filament axis, represented in yellow for vertically-oriented and in blue for horizontally-oriented filaments in Fig. 3(b). The transition
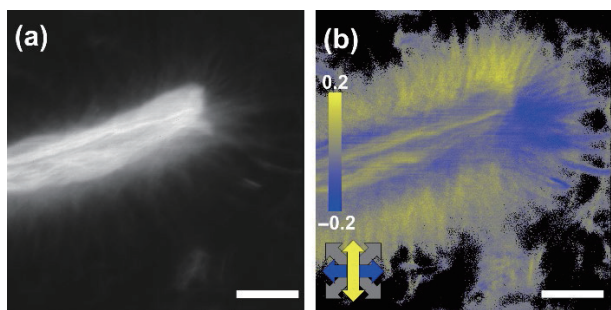
region between the filaments and the core contains the mixture of blue and yellow, showing that some dipoles are oriented vertically and some horizontally. This appears due to several layers of clustered filaments pointing to different directions. Similar filament organization is seen in confocal images (Figs. 1(a) and 1(c)).

3.4 Correlation between SEM and FDLD microscopy data

The dried GSU aggregate was first imaged using FDLD microscopy, and then coated with a 5 nm gold layer and imaged with SEM. The structural images are presented in Fig. 4 and can be directly compared among fluorescence intensity (Fig. 4(a)), FDLD (Fig. 4(b)), and SEM (Figs. 4(c) and 4(d)) images. The SEM images show the tubular central core (Figs. 4(c) and 4(d)). The cracks in the tube reveal multilayer ribbons that coil around the tube axis into a helical structure. A comparison of the dipolar orientations in the FDLD (Fig. 4(b)) images with the SEM (Figs. 4(c) and 4(d)) images reveals layers of the ribbon that correlate with blue or yellow areas in FDLD, showing different orientations of molecules in different layers. Some yellow and blue areas in the FDLD map also correlate with the cracks in the core tube, indicating that fluorescence from the inner parts of the
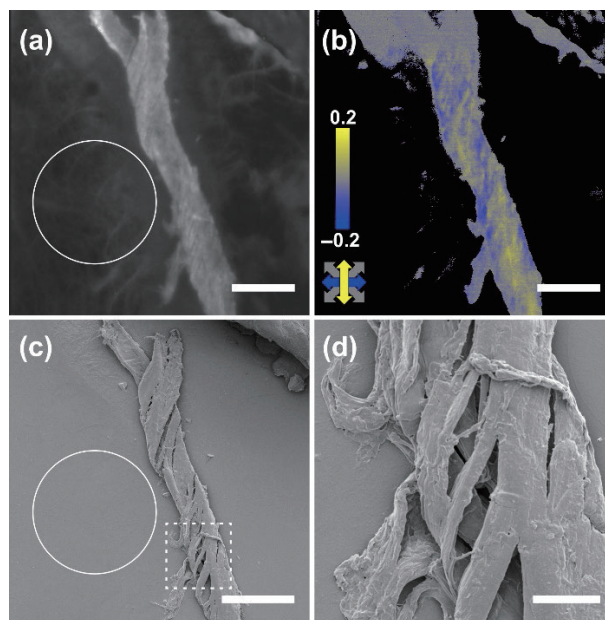

Figure 4 Comparison of fluorescence intensity (a), FDLD (b), and SEM ((c) and (d)) images of a GSU TPPS$_4$ aggregate. The yellow and blue arrows (b) for vertical and horizontal directions, respectively, represent the orientation of absorption dipoles of J-bands. The scale bars are 50 μm in (a)–(c) and 10 μm in (d). The central core tube composed of ribbons helically wound around the core axis (d). The small filaments can be seen at the substrate level within white circle in (a) and (c).

Figure 3 Fluorescence-detected polarization microscopy of the GSU TPPS$_4$ aggregate. Fluorescence intensity (a) and FDLD (b) images of the GSU aggregate. Yellow and blue colors represent vertical and horizontal orientations of the absorption dipoles, respectively, as indicated by the arrows in (b). Scale bars: 25 μm.

ribbon also originates from aligned dipoles.

The filaments that attach to the central tube are very thin; therefore, during drying and coating for SEM they detach and flatten on the substrate (see the encircled area in Figs. 4(a) and 4(c)). The filaments crisscross in the same way as in the AFM images presented in the next section.

3.5 Atomic force microscopy

A detailed structure of GSU aggregates was examined at high resolution with atomic force microscope. The GSU aggregates were dried on a glass substrate. Figure 5 shows AFM images of the surface structure of central core (Figs. 5(a) and 5(b)) and the dried filaments on substrate near the central core (Figs. 5(c) and 5(d)).
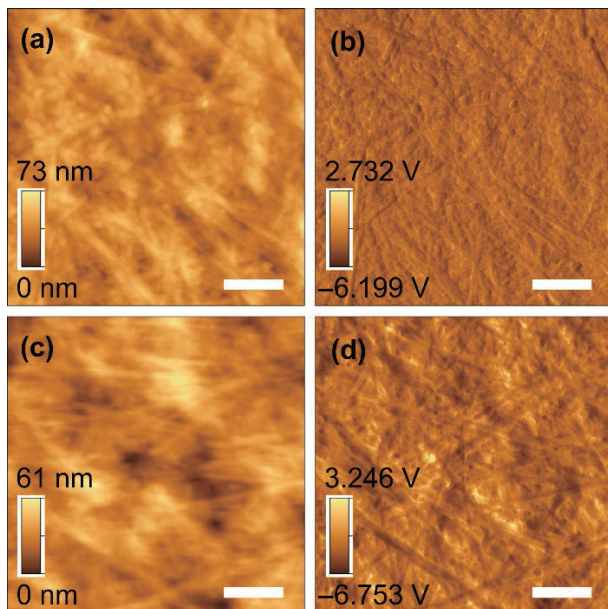
Figure 5 AFM images of GSU core surface ((a) and (b)) and filaments dried on the substrate near the core region ((c) and (d)). The height images ((a) and (c)) and the phase images ((b) and (d)) are presented. Scale bars: 1 μm.

The central core surface shows granulated structure with some flattened filaments emerging from the core at different directions (Figs. 5(a) and 5(b)). The filaments crisscross on the top of each other without branching. The characteristic size of the nanogranules is about 120 ± 5 nm, while the diameter of individual filament is 70 ± 5 nm.

The filaments on the glass substrate (Figs. 5(c) and 5(d)) also crisscross on top of each other. The filaments on the glass substrate, shown in Fig. 5(c), have similar diameter as ones on the core surface (Fig. 5(a)). Similar crisscrossing filament structures were observed with AFM for a film of TPPS$_4$ J-aggregates deposited on a substrate for humidity sensor applications [43].

There are only a few nanogranular structures visible in the filament region. The nanogranular or flocculated structures attached to the nanotubes have been observed previously for TPPS$_4$ J-aggregates dried on the substrate [6]. In this work, we demonstrate that nanogranular and filamentous nanostructures form microscopic core. In addition, the long filaments attach to the core forming the peculiar hierarchical superstructures of GSU aggregates.

3.6 Second- and third-harmonic generation microscopy

Multimodal SHG and THG microscopy was used to image the 3D structure of wet GSU aggregate (Fig. 6 and Movie ESM1). SHG indicates that the filaments are noncentrosymmetric, while THG arises due to the refractive index and susceptibility mismatch between the filaments and the mounting gel medium. The image shows bundled filaments (Figs. 6(a) and 6(c)). The harmonic
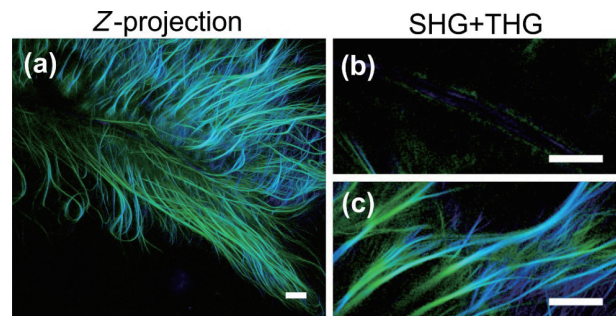

Figure 6 3D organization of GSU TPPS$_4$ aggregate in polyacrylamide gel imaged with SHG (green) and THG (blue) microscopy. Maximum axial projection (a), 3D rendering movie shown in Movie ESM1. Optical section of the central core (b) and the filaments (c). Scale bars: 50 μm.

signals of the filaments decrease towards the center due to crisscrossing of the fibers in focal volumes. The core itself gives almost no SHG signal (except at the surface (Fig. 6(b))), which indicates close to centrosymmetric organization of chromophores. The THG signal from the core inner volume is low. It highlights longitudinal structures, most probably, from the inner surface of the core tube, and also from the cracks and interfaces between the ribbons constituting the tube.

3.7 Polarimetric SHG microscopy

The ultrastructure of GSU aggregates is investigated using PIPO SHG microscopy [53]. Multiple optical sections recorded at three different heights are presented in Fig. 7. The SHG intensity images highlight the filaments. The core has very low signal, however, some structures are visible indicating that it is not completely hollow (column 1 in Fig. 7).

The polarization properties of the SHG signal provide ultrastructural information. The achiral susceptibility ratio R in the molecular frame can be expressed as follows [41]

$$R = \frac{\chi^{(2)}_{zzz}}{\chi^{(2)}_{zxx}}\cos^2\alpha + \left(1 + 2\frac{\chi^{(2)}_{xxz}}{\chi^{(2)}_{zxx}}\right)\sin^2\alpha \tag{1}$$

The R ratio depends on the achiral susceptibility tensor elements $\chi^{(2)}_{zzz}$, $\chi^{(2)}_{zxx}$, and $\chi^{(2)}_{xxz}$, where the z axis is along and the x, y axes are perpendicular to the fiber, and α is the out-of the image plane tilt angle. The R-ratios from the core areas are similar to the filaments (column 2 in Fig. 7). Most likely those pixels show signal from the filamentous aggregates incorporated into the core. The R ratio for the filaments has a very large range from 1.5 up to 7.5. This appears due to α tilt angle (see Eq. (1)), and due to crossing fibers in a focal volume, clearly seen in Fig. S11 in the ESM.

The C-ratio maps presented in column 3 in Fig. 7 show the zones of positive and negative values, providing evidence for chiral arrangement of the filaments. The C-ratio is

$$C = \frac{\chi^{(2)}_{xyz}}{\chi^{(2)}_{zxx}}\sin\alpha \tag{2}$$

where $\chi^{(2)}_{xyz}$ is the chiral susceptibility tensor component. If a chiral fiber is imaged lying in the image plane, or several chiral fibers are symmetrically tilted up and down with respect to the image plane (in the same focal volume), then the C-ratio is zero.

The filaments of the GSU aggregates exhibit strong chirality, which is estimated to be around $\chi^{(2)}_{xyz}/\chi^{(2)}_{zxx} = 0.6$ using Eq. (2) and data from the C-ratio images at three different depths. The C-ratio maps show zones of positive and negative values. The sign of the C-ratio depends on the handedness and the out-of-plane tilt angle according to Eq. (2). Thus, the tilt orientation of clusters could be the same, but with the opposite chirality.

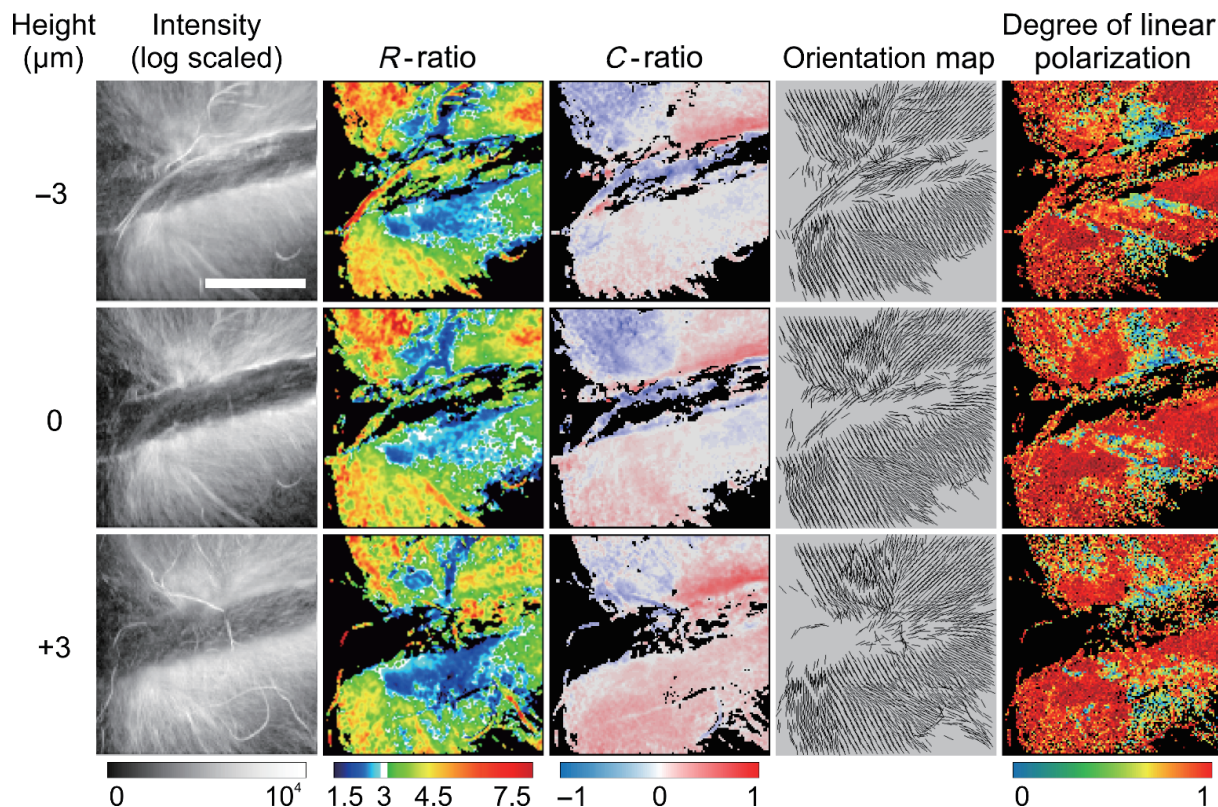Alternatively, the same chirality fibers could be clustered with

Figure 7 Polarimetric SHG images of GSU TPPS$_4$ aggregates at three different depths. Rows represents P-SHG images at −3, 0, and +3 μm depth (top to bottom). SHG intensity is shown in column 1, *R*- and *C*- ratio maps in columns 2 and 3, respectively, orientation maps of voxel's effective cylindrical axis in column 4, and the DLP maps in column 5. Scale bar: 50 μm.

layers pointing up and down from the image plane. The values of the *C*-ratio in the images have a broad distribution, indicating that the chirality of the filaments is higher than, for example, that of collagen [41, 58]. The clustered areas of filaments show a homogeneous *C*-ratio, meaning that filaments are of the same chirality within the cluster, and are attached to the central core with the same polarity and the same out-of-plane orientation.

The molecular frame *R*- and *C*-ratios are determined for each pixel, therefore, the two ratio images can be correlated. The $\chi^{(2)}_{zzz}/\chi^{(2)}_{zxx}$ of an individual fiber can be best determined from the pixels with *C* = 0, and where there is no crossing of the fibers. The estimated ratio $\chi^{(2)}_{zzz}/\chi^{(2)}_{zxx}$ = 6.5. Such high $\chi^{(2)}_{zzz}/\chi^{(2)}_{zxx}$ observed, e.g., in starch granules [59] and β-carotene aggregates [40].

The orientation maps representing the effective in-plane angle of the cylindrical axis of each focal volume show that filaments are oriented at an angle with respect to the normal of the central core axis (column 4 in Fig. 7). The angle can be positive or negative for different clustered layers of the filaments, while inside the clusters the filaments orient parallel to each other. Correlation of the orientation maps and *C*-ratio maps shows that clusters can cross at different heights and each cluster is pointing with a specific *α* tilt angle, and has the same chirality.

The degree of linear polarization (DLP) maps show the per-pixel polarization purity of the SHG signal (column 5 in Fig. 7). If SHG signal in a pixel originates from a single filament or unidirectionally ordered cluster of the filaments, the polarization purity is high and the DLP value is close to 1. If the filaments cross each other within a single focal volume, a lower DLP value is expected. High DLP values in Fig. 7 show that some clusters of the filaments are unidirectionally oriented in the GSU aggregates.

4 Discussion

4.1 Structure and self-assembly of the GSU aggregate

The central core and the filaments of a GSU aggregate self-

assemble from the same zwitterionic TPPS$_4$ molecules, yet they exhibit different spectroscopic properties and different macrostructural as well as ultrastructural arrangements. This is possible when molecules aggregate into several distinct ultrastructural organizations coexisting in the same solution. The initial assemblies of nucleation centers with different configurations determine the fate of aggregate structures, e.g., forming flocculated (nanogranular) and filamentous aggregates. Further, different types of aggregates assemble via specific interactions into tubular cores and filaments, and form giant supramolecular assemblies. The assemblies can assume peculiar forms, one example being the giant sea urchin aggregate. Previously, we also observed large network-like structures arranged from the fibers of TPPS$_4$ J-aggregates [6].

4.2 Structure of the central core

Imaging of the GSU TPPS$_4$ aggregates with different microscopy modalities reveals a tubular structure of the central core. The core tube structural models are presented in Fig. 8. The central tube has rough and granulated surface observed with AFM (Fig. 8(a)), and is composed of ribbons (Fig. 8(b)) either assembled straight (Fig. 8(c)) or helically wound around the central axis of the tube (Fig. 8(d)) as revealed by SEM. The ribbons are composed of layers consisting of aggregates with J- and H- bands of fluorescence.

In addition, red shifted fluorescing species with bands at 743 and 768 nm have characteristic presence in the central core, which might be associated with specific aggregate forms, e.g., nanogranular aggregates observed by AFM. The absorption dipole orientation varies along the tube, and correlation of FDLD and SEM images indicates different orientations of the dipoles in different ribbon layers, leading to stripy appearance of the core tube in FDLD images. The low SHG intensity in the core shows close to centrosymmetric organization of nonlinear dipoles. The centrosymmetric arrangement can be achieved by different layers
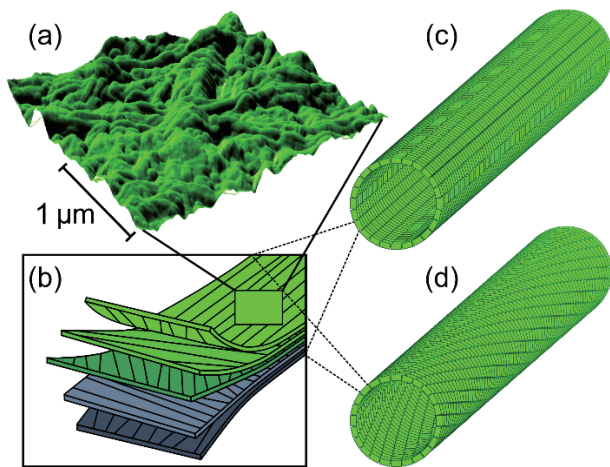
Figure 8 Structural model of the GSU central core. The granulated surface topography observed with AFM microscopy (a), scale bar: 1 μm. A multilayer ribbon structure deduced from SEM and FDLD (b). A central core tube made of straight ribbons (c) and helically arranged ribbons (d).

having different molecular orientations.

4.3 Structure of the filaments

Imaging with 488 nm excitation reveals the filaments containing spectral pattern of TPPS$_4$ J-aggregate. The fluorescence spectra show that it is also connected to pattern of H-aggregate. The FDLD and SHG polarization data demonstrate that the linear and nonlinear dipoles of J-aggregates are oriented along the filament axis, and the filaments can be described by C$_\infty$ symmetry. The alignment of the J-aggregate dipoles along the filament axis excludes the model of TPPS$_4$ molecular orientation with dipoles perpendicular to the filament axis.

There are two possible models of TPPS$_4$ molecular arrangements forming the nanotubes with dipoles oriented along the filament axis (see Fig. 9). Nanotubes can be formed from TPPS$_4$ molecules with either "adjacent" or the "opposite" negatively charged sulfo- groups, respectively (Figs. 9(a) and 9(b)).

(i) The face-exposed model (Figs. 9(c) and 9(e)) has the "adjacent" TPPS$_4$ molecules oriented with the planar face towards the nanotube surface [60–62]. (ii) The edge-exposed model (Figs. 9(d) and 9(f)) has the "opposite" TPPS$_4$ molecules stacked together with the edge exposed to the nanotube surface [4, 63]. In both cases, the molecular dipoles have a slight tilt out of the surface of the cylinder giving ratio $\chi^{(2)}_{zzz}/\chi^{(2)}_{zxx} = 6.5$, and are twisted around the nanotube axis giving chiral ratio $\chi^{(2)}_{xyz}/\chi^{(2)}_{zxx} = 0.6$.

The unit sphere representation of nonlinear susceptibility tensor of the nanotube oriented along z axis is presented in Figs. 9(g) and 9(h). It shows arrangement of nonlinear dipoles along the nanotube with small tilt angle from z axis (Fig. 9(h)), and with a curl due to nanotube chirality (Figs. 9(g) and 9(h)). The nanotube can have left or right chiral organization.

4.4 Varying attachment angle of the filament clusters to the core surface

The connection between the central core and the filaments appears at different angles. However, a cluster or layer of filaments is attached with the same angle to the core. Several geometrical constrains can lead to such arrangement. The nanotubes of the filaments can be achiral or chiral and therefore respectively have terminating plane either perpendicular to the surface of the filament or at an angle corresponding to the pitch angle and left- or right-handedness of the helix. Therefore, the filament attachment angle depends on the chirality of nanotube. In addition, specific interactions may occur between the neighboring
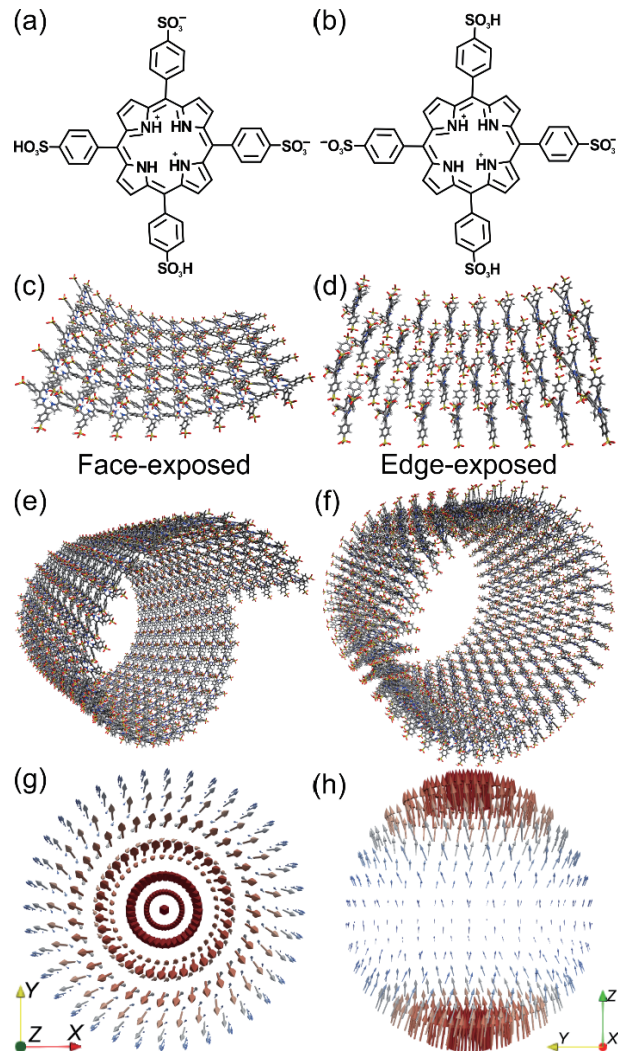

Figure 9 Structural models of GSU filaments. TPPS$_4$ monomers with "adjacent" (a) and "opposite" (b) negatively charged sulfo- groups. The 3D view of the filament surface patch and the filaments for face-exposed ((c), (e), and Model ESM2) and edge-exposed ((d), (f), and Model ESM3) molecular models of the TPPS$_4$ nanotube. The unit sphere representation of nonlinear susceptibility tensor of the nanotube oriented along z-axis, top view (g) and side view (h). The nanotubes are shown with one handedness, but can assume also the opposite.

filaments. The imposed geometrical constrains lead to selective clustering of filaments with the same chirality. The CD signal of the bulk solution containing GSU aggregates does not have prevailing signal of one chirality, indicating towards the racemic mixtures. Therefore, different clusters might be of different chirality, but within the individual cluster the filaments associate selectively of the same chirality.

4.5 Energy transfer in GSU aggregates

The TPPS$_4$ aggregates resemble bacterial light harvesting photosynthetic pigment aggregates contained in the chlorosomes of green sulfur bacteria [21, 64]. The observed variations in fluorescence spectra and lifetimes of GSU aggregate reveal energy transfer between molecular patterns of J- and H-aggregates, and red-shifted fluorescing species. The filaments have intense fluorescence and a few nanosecond fluorescence lifetimes, which get highly quenched in the dry aggregates due to packing of the filaments on the substrate. Packing facilitates energy transfer between the filaments, leading to efficient quenching. The energy transfer within filaments and connectivity between them can be potentially utilized for efficient light-harvesting. Therefore, GSU

aggregates are promising structures for application of light-harvesting in artificial photosynthesis.

5   Conclusions

By using a range of spectroscopic and polarimetric microscopy techniques we reveal that zwitterionic TPPS$_4$ molecules self-assemble into giant sea urchin type aggregates showing characteristic spectral patterns of J- and H-aggregates as well as red shifted fluorescing species formed in acidic solution. Those aggregates further assemble into nanotubular and nanogranular structures, which in turn form non-branching chiral filaments and microscopic tubular core structures comprised of multilayer ribbons. The filaments of the same chirality and polarity cluster together and attach to the core forming the filament layers. We describe the principles of self-assembly of GSU aggregates, which thus lay the foundation for possible design and control of giant aggregate self-assembly that can result in different functional properties of the nano- and micro-structures. The control of self-assembly has a potential for applications in various fields including nanotechnology, nonlinear microscopy, and artificial photosynthesis.

Acknowledgements

Electronic Supplementary Material: Supplementary material (supplemental data and result analysis;
Movie ESM1. Rotating 3D reconstruction of the GSU aggregate. Imaging was performed using multimodal SHG and THG microscopy. Green color represents SHG signal and blue color—THG. The same data set is used in Fig. 6;
Model ESM2. 3D model of the filament for face-exposed molecular TPPS$_4$ nanotube in a.cml file format;
Model ESM3. 3D model of the filament for edge-exposed molecular TPPS$_4$ nanotube in a.cml file format) is available in the online version of this article at https://doi.org/10.1007/s12274-021-4048-x.

References

[1]   Tirard, S. Abiogenesis. In *Encyclopedia of Astrobiology*. Gargaud, M.; Irvine, W. M.; Amils, R.; Claeys, P.; Cleaves, H. J.; Gerin, M.; Rouan, D.; Spohn, T.; Tirard, S.; Viso, M., Eds.; Springer: Berlin, Heidelberg, 2014.

[2]   Ohno, O.; Kaizu, Y.; Kobayashi, H. *J*-aggregate formation of a water-soluble porphyrin in acidic aqueous media. *J. Chem. Phys.* **1993**, *99*, 4128–4139.

[3]   Maiti, N. C.; Mazumdar, S.; Periasamy, N. J-and H-aggregates of porphyrin-surfactant complexes: Time-resolved fluorescence and other spectroscopic studies. *J. Phys. Chem. B* **1998**, *102*, 1528–1538.

[4]   Short, J. M.; Berriman, J. A.; Kübel, C.; El-Hachemi, Z.; Naubron, J. V.; Balaban, T. S. Electron cryo-microscopy of TPPS$_4$·2HCl tubes reveals a helical organisation explaining the origin of their chirality. *ChemPhysChem* **2013**, *14*, 3209–3214.

[5]   Kobayashi, T. *J-Aggregates*; World Scientific: Singapore, 2012.

[6]   Rotomskis, R.; Augulis, R.; Snitka, V.; Valiokas, R.; Liedberg, B. Hierarchical structure of TPPS$_4$ J-aggregates on substrate revealed by atomic force microscopy. *J. Phys. Chem. B* **2004**, *108*, 2833–2838.

[7]   Ribó, J. M.; Crusats, J.; Sagués, F.; Claret, J.; Rubires, R. Chiral sign induction by vortices during the formation of mesophases in stirred solutions. *Science* **2001**, *292*, 2063–2066.

[8]   Aggarwal, L. P. F.; Borissevitch, I. E. On the dynamics of the TPPS$_4$ aggregation in aqueous solutions: Successive formation of H and J aggregates. *Spectrochim. Acta Part A: Mol. Biomol. Spectrosc.* **2006**, *63*, 227–233.

[9]   Romeo, A.; Castriciano, M. A.; Zagami, R.; Pollicino, G.; Scolaro, L. M.; Pasternack, R. F. Effect of zinc cations on the kinetics of supramolecular assembly and the chirality of porphyrin J-aggregates. *Chem. Sci.* **2017**, *8*, 961–967.

[10]   Chen, X. D.; Liu, M. H. Induced chirality of binary aggregates of oppositely charged water-soluble porphyrins on DNA matrix. *J. Inorg. Biochem.* **2003**, *94*, 106–113.

[11]   Liao, B.; He, B. Q.; Liu, R. G.; Huang, Y. Induced circular dichroism of anionic porphyrin TPPS aggregates in DNA solutions. *Polym. J.* **2009**, *41*, 739–743.

[12]   Randazzo, R.; Gaeta, M.; Gangemi, C. M. A.; Fragalà, M. E.; Purrello, R.; D'Urso, A. Chiral recognition of L- and D- amino acid by porphyrin supramolecular aggregates. *Molecules* **2019**, *24*, 84.

[13]   Zhao, L. Z.; Xiang, R.; Ma, R. J.; Wang, X.; An, Y. L.; Shi, L. Q. Chiral conversion and memory of TPPS J-aggregates in complex micelles: PEG-*b*-PDMAEMA/TPPS. *Langmuir* **2011**, *27*, 11554–11559.

[14]   Koti, A. S. R.; Periasamy, N. Self-assembly of template-directed J-aggregates of porphyrin. *Chem. Mater.* **2003**, *15*, 369–371.

[15]   Fukushima, Y. Interaction of porphyrin derivatives with a β-sheet structure of a zwitterionic polypeptide in aqueous solution. *Polym. Bull.* **2001**, *45*, 479–485.

[16]   Wang, Q. L.; Zhang, L.; Yang, D.; Li, T. S.; Liu, M. H. Chiral signs of TPPS co-assemblies with chiral gelators: Role of molecular and supramolecular chirality. *Chem. Commun.* **2016**, *52*, 12434–12437.

[17]   Rong, Y. L.; Chen, P. L.; Liu, M. H. Self-assembly of water-soluble TPPS in organic solvents: From nanofibers to mirror imaged chiral nanorods. *Chem. Commun.* **2013**, *49*, 10498–10500.

[18]   Lauceri, R.; Purrello, R. Transfer, memory and amplification of chirality in porphyrin aggregates. *Supramol. Chem.* **2005**, *17*, 61–66.

[19]   Rimeika, R.; Čiplys, D.; Poderys, V.; Rotomskis, R.; Balakauskas, S.; Shur, M. S. Subsecond-response SAW humidity sensor with porphyrin nanostructure deposited on bare and metallised piezoelectric substrate. *Electron. Lett.* **2007**, *43*, 1055–1057.

[20]   Schwab, A. D.; Smith, D. E.; Bond-Watts, B.; Johnston, D. E.; Hone, J.; Johnson, A. T.; de Paula, J. C.; Smith, W. F. Photoconductivity of self-assembled porphyrin nanorods. *Nano Lett.* **2004**, *4*, 1261–1265.

[21]   Chappaz-Gillot, C.; Marek, P. L.; Blaive, B. J.; Canard, G.; Bürck, J.; Garab, G.; Hahn, H.; Jávorfi, T.; Kelemen, L.; Krupke, R. et al. Anisotropic organization and microscopic manipulation of self-assembling synthetic porphyrin microrods that mimic chlorosomes: Bacterial light-harvesting systems. *J. Am. Chem. Soc.* **2012**, *134*, 944–954.

[22] Zhao, Q.; Wang, Y.; Xu, Y. S.; Yan, Y.; Huang, J. B. Out-of-plane coordinated porphyrin nanotubes with enhanced singlet oxygen generation efficiency. *Sci. Rep.* **2016**, *6*, 31339.

[23] Hilmey, D. G.; Abe, M.; Nelen, M. I.; Stilts, C. E.; Baker, G. A.; Baker, S. N.; Bright, F. V.; Davies, S. R.; Gollnick, S. O.; Oseroff, A. R. et al. Water-soluble, core-modified porphyrins as novel, longer-wavelength-absorbing sensitizers for photodynamic therapy. II. Effects of core heteroatoms and *meso*-substituents on biological activity. *J. Med. Chem.* **2002**, *45*, 449–461.

[24] Micali, N.; Villari, V.; Scolaro, L. M.; Romeo, A.; Castriciano, M. A. Light scattering enhancement in an aqueous solution of spermine-induced fractal J-aggregate composite. *Phys. Rev. E* **2005**, *72*, 050401.

[25] Scolaro, L. M.; Romeo, A.; Castriciano, M. A.; Micali, N. Unusual optical properties of porphyrin fractal J-aggregates. *Chem. Commun.* **2005**, 3018–3020.

[26] Takechi, H.; Canillas, A.; Ribó, J. M.; Watarai, H. Alignment and chirality of porphyrin J aggregates formed at the liquid–liquid interface of a centrifugal liquid membrane cell. *Langmuir* **2013**, *29*, 7249–7256.

[27] Vaz Serra, V.; Neto, N. G. B.; Andrade, S. M.; Costa, S. M. B. Core-assisted formation of porphyrin J-aggregates in pH-sensitive polyelectrolyte microcapsules followed by fluorescence lifetime imaging microscopy. *Langmuir* **2017**, *33*, 7680–7691.

[28] Zagami, R.; Castriciano, M. A.; Romeo, A.; Trapani, M.; Pedicini, R.; Scolaro, L. M. Tuning supramolecular chirality in *nano* and mesoscopic porphyrin J-aggregates. *Dyes Pigm.* **2017**, *142*, 255–261.

[29] Kim, T.; Ham, S.; Lee, S. H.; Hong, Y.; Kim, D. Enhancement of exciton transport in porphyrin aggregate nanostructures by controlling the hierarchical self-assembly. *Nanoscale* **2018**, *10*, 16438–16446.

[30] Aziz, A.; Narasimhan, K. L.; Periasamy, N.; Maiti, N. C. Electrical and optical properties of porphyrin monomer and its J-aggregate. *Philos. Mag. B* **1999**, *79*, 993–1004.

[31] Ma, H. L.; Jin, W. J. Studies on the effects of metal ions and counter anions on the aggregate behaviors of *meso*-tetrakis(*p*-sulfonatophenyl)porphyrin by absorption and fluorescence spectroscopy. *Spectrochim. Acta Part A: Mol. Biomol. Spectrosc.* **2008**, *71*, 153–160.

[32] Morgan, C. G.; Mitchell, A. C.; Murray, J. G. *Nanosecond Time-Resolved Fluorescence Microscopy - Principles and Practice*; Adam Hilger Ltd: Bristol, 1990 pp 463–466.

[33] Buurman, E. P.; Sanders, R.; Draaijer, A.; Gerritsen, H. C.; van Veen, J. J. F.; Houpt, P. M.; Levine, Y. K. Fluorescence lifetime imaging using a confocal laser scanning microscope. *Scanning* **1992**, *14*, 155–159.

[34] Gerritsen, H. C.; Draaijer, A.; van den Heuvel, D. J.; Agronskaia, A. V. Fluorescence lifetime imaging in scanning microscopy. In *Handbook of Biological Confocal Microscopy*. Pawley, J. B., Ed.; Springer: Boston, MA, 2006; pp 516–534.

[35] Barzda, V.; de Grauw, C. J.; Vroom, J.; Kleima, F. J.; van Grondelle, R.; van Amerongen, H.; Gerritsen, H. C. Fluorescence lifetime heterogeneity in aggregates of LHCII revealed by time-resolved microscopy. *Biophys. J.* **2001**, *81*, 538–546.

[36] Garab, G.; Pomozi, I.; Weiss, G.; Jörgens, R. Method and apparatus for determining the polarization properties of light emitted, reflected or transmitted by a material using a laser scanning microscope. U. S. Patent 6856391, July 17, 2002.

[37] Steinbach, G.; Pomozi, I.; Zsiros, O.; Menczel, L.; Garab, G. Imaging anisotropy using differential polarization laser scanning confocal microscopy. *Acta Histochem.* **2009**, *111*, 317–326.

[38] Steinbach, G.; Pawlak, K.; Pomozi, I.; Tóth, E. A.; Molnár, A.; Matkó, J.; Garab, G. Mapping microscopic order in plant and mammalian cells and tissues: Novel differential polarization attachment for new generation confocal microscopes (DP-LSM). *Methods Appl. Fluoresc.* **2014**, *2*, 015005.

[39] Sandkuijl, D.; Tuer, A. E.; Tokarz, D.; Sipe, J. E.; Barzda, V. Numerical second-and third-harmonic generation microscopy. *J. Opt. Soc. Am. B* **2013**, *30*, 382–395.

[40] Tokarz, D.; Cisek, R.; Krouglov, S.; Kontenis, L.; Fekl, U.; Barzda,

V. Molecular organization of crystalline β-carotene in carrots determined with polarization-dependent second and third harmonic generation microscopy. *J. Phys. Chem. B* **2014**, *118*, 3814–3822.

[41] Golaraei, A.; Mirsanaye, K.; Ro, Y.; Krouglov, S.; Akens, M. K.; Wilson, B. C.; Barzda, V. Collagen chirality and three-dimensional orientation studied with polarimetric second-harmonic generation microscopy. *J. Biophotonics* **2019**, *12*, e201800241.

[42] Tokarz, D.; Cisek, R.; Golaraei, A.; Asa, S. L.; Barzda, V.; Wilson, B. C. Ultrastructural features of collagen in thyroid carcinoma tissue observed by polarization second harmonic generation microscopy. *Biomed. Opt. Express* **2015**, *6*, 3475–3481.

[43] Rimeika, R.; Rotomskis, R.; Poderys, V.; Čiplys, D.; Sereika, A.; Selskis, A.; Shur, M. S. Surface acoustic wave interaction with humidity-sensitive TPPS4 nano-strip structure. *Ultragarsas* **2006**, *58*, 13–15.

[44] Salomon, A.; Genet, C.; Ebbesen, T. W. Molecule-light complex: Dynamics of hybrid molecule-surface plasmon states. *Angew. Chem., Int. Ed.* **2009**, *48*, 8748–8751.

[45] Jurow, M.; Schuckman, A. E.; Batteas, J. D.; Drain, C. M. Porphyrins as molecular electronic components of functional devices. *Coord. Chem. Rev.* **2010**, *254*, 2297–2310.

[46] Tokarz, D. B. Nonlinear optical properties of carotenoid and chlorophyll harmonophores. Ph. D. Dissertation, University of Toronto, Toronto, 2014.

[47] Cui, L. Y.; Tokarz, D.; Cisek, R.; Ng, K. K.; Wang, F.; Chen, J.; Barzda, V.; Zheng, G. Organized aggregation of porphyrins in lipid bilayers for third harmonic generation microscopy. *Angew. Chem., Int. Ed.* **2015**, *54*, 13928–13932.

[48] Osváth, S.; Meszéna, G.; Barzda, V.; Garab, G. Trapping magnetically oriented chloroplast thylakoid membranes in gels for electric measurements. *J. Photochem. Photobiol. B: Biol.* **1994**, *26*, 287–292.

[49] Schneider, C. A.; Rasband, W. S.; Eliceiri, K. W. NIH image to ImageJ: 25 years of image analysis. *Nat. Methods* **2012**, *9*, 671–675.

[50] Steinbach, G.; Nagy, D.; Sipka, G.; Manders, E.; Garab, G.; Zimányi, L. Fluorescence-detected linear dichroism imaging in a re-scan confocal microscope equipped with differential polarization attachment. *Eur. Biophys. J.* **2019**, *48*, 457–463.

[51] De Luca, G. M. R.; Breedijk, R. M. P.; Brandt, R. A. J.; Zeelenberg, C. H. C.; de Jong, B. E.; Timmermans, W.; Azar, L. N.; Hoebe, R. A.; Stallinga, S.; Manders, E. M. M. Re-scan confocal microscopy: Scanning twice for better resolution. *Biomed. Opt. Express* **2013**, *4*, 2644–2656.

[52] Schindelin, J.; Arganda-Carreras, I.; Frise, E.; Kaynig, V.; Longair, M.; Pietzsch, T.; Preibisch, S.; Rueden, C.; Saalfeld, S.; Schmid, B. et al. Fiji: An open-source platform for biological-image analysis. *Nat. Methods* **2012**, *9*, 676–682.

[53] Tuer, A. E.; Krouglov, S.; Prent, N.; Cisek, R.; Sandkuijl, D.; Yasufuku, K.; Wilson, B. C.; Barzda, V. Nonlinear optical properties of type I collagen fibers studied by polarization dependent second harmonic generation microscopy. *J. Phys. Chem. B* **2011**, *115*, 12759–12769.

[54] Major, A.; Cisek, R.; Barzda, V. Femtosecond Yb: KGd(WO$_4$)$_2$ laser oscillator pumped by a high power fiber-coupled diode laser module. *Opt. Express* **2006**, *14*, 12163–12168.

[55] Hanwell, M. D.; Curtis, D. E.; Lonie, D. C.; Vandermeersch, T.; Zurek, E.; Hutchison, G. R. Avogadro: An advanced semantic chemical editor, visualization, and analysis platform. *J. Cheminform.* **2012**, *4*, 17.

[56] Kelbauskas, L.; Bagdonas, S.; Dietel, W.; Rotomskis, R. Excitation relaxation and structure of TPPS$_4$ J-aggregates. *J. Luminescence* **2003**, *101*, 253–262.

[57] Barzda, V.; Jennings, R. C.; Zucchelli, G.; Garab, G. Kinetic analysis of the light-induced fluorescence quenching in light-harvesting chlorophyll *a/b* pigment-protein complex of photosystem II. *Photochem. Photobiol.* **1999**, *70*, 751–759.

[58] Golaraei, A.; Kontenis, L.; Mirsanaye, K.; Krouglov, S.; Akens, M. K.; Wilson, B. C.; Barzda, V. Complex susceptibilities and chiroptical effects of collagen measured with polarimetric second-harmonic generation microscopy. *Sci. Rep.* **2019**, *9*, 12488.

[59] Cisek, R.; Tokarz, D.; Krouglov, S.; Steup, M.; Emes, M. J.; Tetlow, I. J.; Barzda, V. Second harmonic generation mediated by aligned water in starch granules. *J. Phys. Chem. B* **2014**, *118*, 14785–14794.

[60] Friesen, B. A.; Nishida, K. R. A.; McHale, J. L.; Mazur, U. New nanoscale insights into the internal structure of tetrakis(4-sulfonatophenyl) porphyrin nanorods. *J. Phys. Chem. C* **2009**, *113*, 1709–1718.

[61] Vlaming, S. M.; Augulis, R.; Stuart, M. C. A.; Knoester, J.; van Loosdrecht, P. H. M. Exciton spectra and the microscopic structure of self-assembled porphyrin nanotubes. *J. Phys. Chem. B* **2009**, *113*, 2273–2283.

[62] Wan, Y.; Stradomska, A.; Fong, S.; Guo, Z.; Schaller, R. D.; Wiederrecht, G. P.; Knoester, J.; Huang, L. B. Exciton level structure and dynamics in tubular porphyrin aggregates. *J. Phys. Chem. C* **2014**, *118*, 24854–24865.

[63] Leishman, C. W.; McHale, J. L. Illuminating excitonic structure in ion-dependent porphyrin aggregates with solution phase and single-particle resonance Raman spectroscopy. *J. Phys. Chem. C* **2016**, *120*, 12783–12795.

[64] Jochum, T.; Reddy, C. M.; Eichhöfer, A.; Buth, G.; Szmytkowski, J.; Kalt, H.; Moss, D.; Balaban, T. S. The supramolecular organization of self-assembling chlorosomal bacteriochlorophyll *c*, *d*, or *e* mimics. *Proc. Natl. Acad. Sci. USA* **2008**, *105*, 12736–12741.